A sexually dimorphic hepatic cycle of very low density lipoprotein uptake and assembly

Tomaz Martini [1], Cedric Gobet [1], Andrea Salati [1], Jérôme Blanc [2], Aart Mookhoek [3], Graham Knott [2], Jessica Sordet-Dessimoz [4], Felix Naef [1]

[1] Institute of Bioengineering, School of Life Sciences, Ecole Polytechnique Fédérale de Lausanne, Lausanne, Switzerland

[2] Bioelectron Microscopy Core Facility, School of Life Sciences, Ecole Polytechnique Fédérale de Lausanne, Lausanne, Switzerland

[3] Institute of Tissue Medicine and Pathology, University of Bern, Bern, Switzerland

[4] Histology Core Facility, School of Life Sciences, Ecole Polytechnique Fédérale de Lausanne, Lausanne, Switzerland

Correspondence: felix.naef@epfl.ch

Keywords
VLDL, VLDLR, LDL, low density lipoprotein, circadian rhythms, liver zonation, cardiovascular disease, sexual dimorphism, atherosclerosis

ABSTRACT

The liver shows striking sexual dimorphism, which is reflected in differences between women and men in pathologies inherently associated with hepatic function. Recent single-cell transcriptomes revealed spatiotemporal programmes of liver function on the sublobular scale. However, how sexual dimorphism affects this space-time logic remains poorly understood. To address this, we performed single-cell RNA-seq in the mouse liver, which allowed us to model how lobular position, circadian time and sex shape the transcriptome. We found that sex, space and time markedly influence xenobiotic detoxification and lipid processing, including lipoprotein metabolism. Crucially, the very low density lipoprotein receptor (VLDLR) is restricted to the pericentral zone, with significantly higher mRNA and protein levels in female mice, which is conserved in the human liver. In addition, several genes involved in VLDL assembly are periportally biased, and we corroborated periportal VLDL generation with electron microscopy. Together, this suggests a hepatic cycle of periportal formation and pericentral uptake of VLDL. In addition, we demonstrated that in humans VLDLR expression depends also on age and body mass index. Crucially, these processes provide a new window into the sexual dimorphism characterizing atherosclerotic cardiovascular disease.

1. INTRODUCTION

The mammalian liver is a vital metabolic organ, which processes both xenobiotics as well as nutrients, and supplies the body with carbohydrates, proteins and lipids based on recurring daily demands. The liver is the largest gland, and is composed of repetitive units called lobules, with hepatocyte layers organized around a central vein where deoxygenated blood exits. On the opposite side of the lobule, the bile duct, hepatic artery and portal vein form the portal triad. The artery and portal vein deliver oxygen and nutrients, respectively, resulting in nutrient and oxygen gradients along the periportal (PP) to pericentral (PC) axis, leading to differences in hepatocytes along the axis [1]. In addition, the liver also shows striking daily physiological rhythms, which allow it to anticipate and respond to feeding-fasting and activity-rest cycles [2]. Temporal programs are driven by recurring stimuli, such as nutrient availability, and by a genetically encoded molecular clock that drives self-sustained oscillatory processes called circadian rhythms. Taken together, the liver has a strong spatiotemporal organization of physiology [3], and perturbing this organization results in morbidity and mortality [1,4,5]. However, it is not known how spatiotemporal functions are affected by sex beyond bulk and pseudobulk approaches [6–9]. Sex strongly affects the incidence of cancers, including hepatocellular carcinoma (HCC) [10,11], susceptibility to drug adverse effects, including drug-induced liver injury (DILI) [12], as well as major cardiovascular events, with premenopausal women robustly protected against the latter [10]. Moreover, sex differences in cardiovascular disease are amplified with increased dietary fat consumption [10]. Lipoproteins of very low density (VLDL), which supply tissues with triglycerides (TAGs), are the main culprit in atherosclerosis [13–15]. VLDLs mature into intermediate (IDL) and low density lipoproteins (LDL), and are predominantly produced by the liver [16]. In parallel, the liver can turn over a high amount of metabolites due to its size, and has a dominating role in lipid catabolism, enabling it to balance lipoprotein production and lipid degradation. Often, such opposing tasks in the liver are spatiotemporally compartmentalized [1].

Here we found that the VLDL receptor (VLDLR), critically involved in cardiovascular disease [13,17–19], is limited to the pericentral zone, and more highly expressed in females. In parallel, a subset of genes involved in VLDL assembly show higher levels periportally. Electron microscopy (EM) enabled us to confirm that VLDL production shows periportal bias, revealing a previously unknown sexually dimorphic hepatic cycle of periportal formation and pericentral uptake of VLDL. Our results therefore provide novel insights into hepatic lipoprotein homeostasis and sexually dimorphic manifestations of cardiovascular disease.

2. RESULTS

2.1 Single-cell RNA sequencing reveals space, time and sex effects on gene expression in mouse liver

To obtain a first view into the aforementioned sexually dimorphic pathologies, intrinsically tied to the liver, we focused on sets of known pathology-associated genes (S. Table 1) and assessed their sex- and time-dependent expression from liver bulk RNA-seq (SFig. 1). Among the diseases considered, we found differences between the two sexes predominantly in genes associated with cardiovascular disease. Notably, there was higher female expression of *Vldlr*, while the low density lipoprotein receptor (*Ldlr*) and apolipoproteins (*Apo*s) showed comparable expression in both sexes (SFig. 1).

To investigate gene expression in function of time of day, lobular zone and sex, we performed droplet-based scRNA-seq of liver cells, collected, enriched for hepatocytes and cryopreserved at two time points, from male and female mice. The chosen time points, ZT10 and ZT22 (*Zeitgeber time*; ZT0 denotes when the lights are switched on, at ZT12 lights are turned off), correspond to physiologically distinct fasted (ZT10) and fed states (ZT22). Clustering of the cells revealed several nonparenchymal cell types as well as a main cluster of hepatocytes with an expected antizonated *Cyp2e1* (pericentral) and *Cdh1* (periportal) expression (Fig. 1A, SFig. 2A). Based on the clustering, we first assessed effects of time and sex on individual cell types in the pseudobulk, showing both global and cell-type specific regulation (SFig. 2B).

To proceed with the spatial reconstruction of hepatocytes in both sexes, we first showed with immunofluorescence that the canonical parenchymal zonation markers CYP2E1, E-CAD and GLUL exhibited equivalent spatial expression patterns between males and females (Fig. 1B). Additionally, we identified two populations of hepatocytes that differed in the fraction of mitochondrial reads. Hepatocytes with low mitochondrial reads (< 3%) differed markedly in their overall gene expression (SFig. 3) and were therefore not included into the spatial reconstruction. These cells exhibited a downregulation of secreted protein genes, and an upregulation of ribosomal proteins, cytochrome o oxidases, *Jun*, and genes involved in gluconeogenesis [20,21]. Such *mt-Co1*-negative hepatocytes were suggested to represent the liver stem cell niche [22]. For the remaining canonical hepatocytes, we based the spatial reconstruction on a set of established [3,23,24] and robustly detected zonation markers, exhibiting conserved correlation patterns across conditions (SFig. 4). To infer a 1D coordinate for each cell along the central to portal axis, we developed a maximum likelihood approach to directly model the scRNA-seq counts. This revealed a variety of zonated

expression profiles, including ones showing highly robust patterns across conditions, while others exhibited strong differential time and sex effects (Fig. 1C). We then categorized genes into nonzonated or zonated, with the latter accounting for approximately a fifth of the detected genes. These were additionally subcategorized based on effects of sex and time on the spatial expression profiles. More of the zonated genes showed a pericentral bias (Fig. 1D; SFig. 4-5). While sex and time often influence the mean expression levels of zonated genes [7], including metabolic and pathology associated genes (SFig. 5-6), we found that sex or time can also affect the shapes of zonation profiles (Z×S and Z×T, Fig. 1D).

A main goal was to assess sexual dimorphism in zonated metabolic and disease related genes. First, we found that many zonated genes show highly sex-dimorphic mean expression levels (Fig. 1E, SFig. 5). Specifically, we observed major effects of sex on cytochromes (*Cyp*s, SFig. 7), solute carriers (*Slc*s, SFig. 8) and sulfotransferases (*Sult*s, SFig. 9). The strongly sex- [6] and time-dependent [25] zonation profiles of *Cyp*s point to spatiotemporally compartmentalized programmes of xenobiotic biotransformation and drug-induced toxicity [1], which are different in male and female mice. Additionally, *Cyp7a1*, crucial in the neutral pathway of bile acid synthesis, varies with time, and *Cyp7b1*, essential in the acidic pathway of bile acid synthesis, is much higher in males (SFig. 7). Solute carriers, some of which are associated with the sexually disparate DILI [12], show sex-dimorphic and time-of-day regulation, including the pericentral *Slco1a1*, which is higher in males (SFig. 8). Intriguingly, we found with scRNA-seq that the aforementioned *Vldlr* was not only more highly expressed in females, but also pericentrally localized in both sexes (Fig. 1E; SFig. 5).

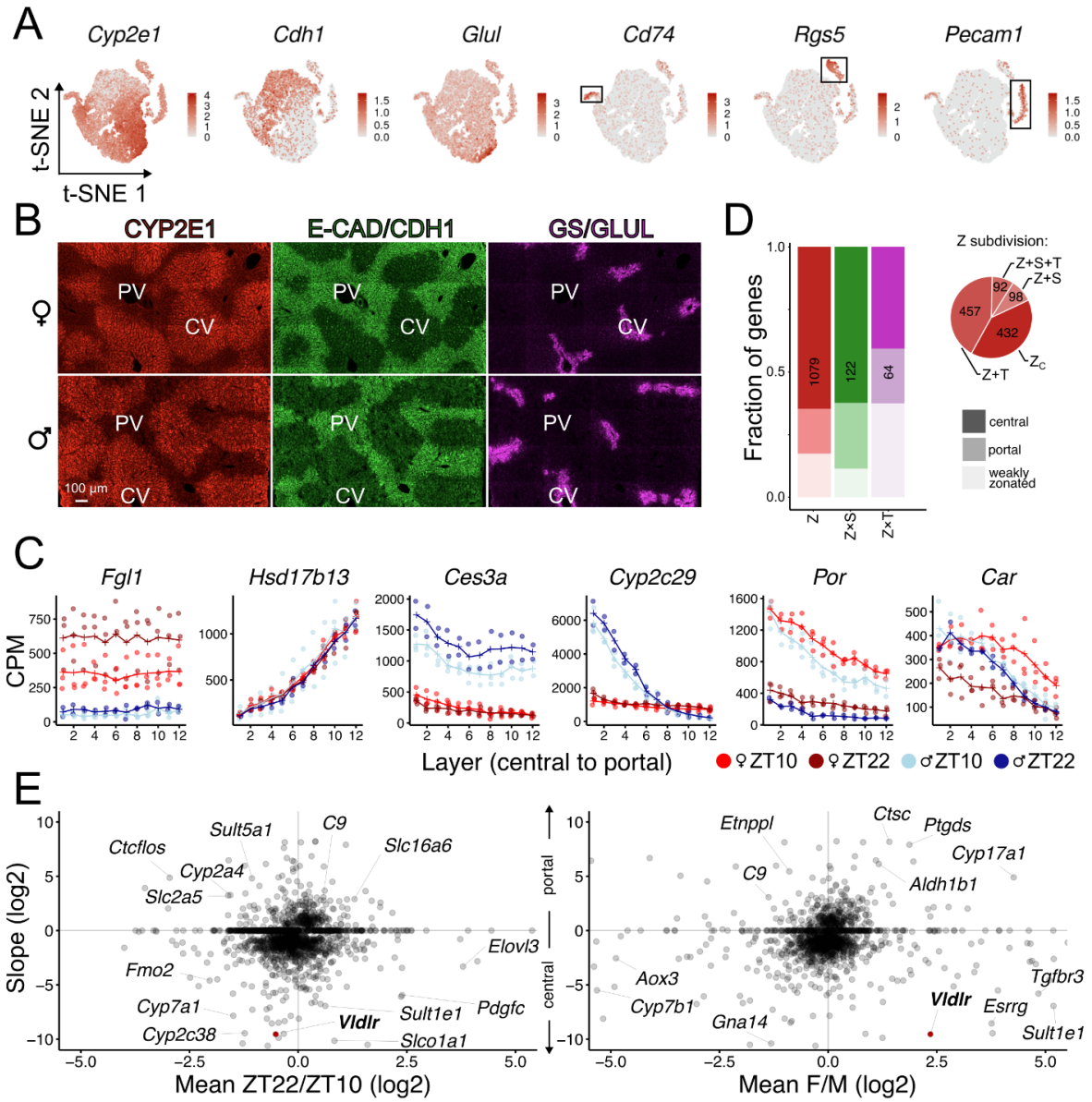

Figure 1: ***scRNA-seq uncovers cell types and the space-, time- and sex-dependent organization of gene expression in mouse liver.*** *(A) t-SNE plots show a main cluster of hepatocytes with antizonated Cyp2e1 and Chd1/Ecad expression, and clusters of non-parenchymal cells identified with marker genes including Rgs5 (stellate cells), Pecam1 (endothelial cells), and Cd74 (immune cells). (B) Spatial patterns of canonical zonation markers E-CAD (periportal), and CYP2E1 and GS/GLUL (both pericentral) are indistinguishable in male and female mice. (C) Reconstructed spatial profiles of gene expression in 12 layers, 1 corresponding to the most pericentral layer. Counts are normalized to the total counts of cytoplasmic unique molecular identifiers (UMI) and represented as counts per million (CPM). Examples include a non-zonated gene (Fgl1; fibrinogen-like 1), and zonated genes, with the slope either not affected by time or sex (Hsd17b13), or with different effects of time and/or sex on the spatial profile in Ces3a (carboxylesterase 3a), Cyp2c29, Por (cytochrome P450 oxidoreductase) and Car/Nr1i3 (constitutive androstane receptor). (D) Spatial reconstructions of lobular mRNA profiles combined with a model selection identified genes differentially affected by time (T), sex (S) and space (Z). The × denotes interacting effects (non-additive in log), resulting in changes of the shape of the spatial profile in function of either time or sex. The group of zonated genes (Z) also includes genes that change their mean*

expression levels with sex or time, but not the shape of zonation (in log), and can be subdivided (pie chart) into genes whose expression is > 50% higher in one sex (Z + S), at one time (Z + T), in function of both sex and time (Z + S + T), or constant across conditions (Z_c). Most zonated genes have a pericentral bias. (E) Sexual dimorphism and temporal changes of zonated genes, represented by the average slope (negative slopes characterize central profiles) across all conditions vs. the ZT22 to ZT10 (left panel) or female to male expression ratio (right panel). Genes in the corners are highly zonated and strongly regulated by time or highly zonated and sexually dimorphic, including Vldlr. Representative genes of functions described in the main text, and genes from S. Table 1 are shown.

2.2 Sexually dimorphic, compartmentalized Vldlr expression and VLDL generation

VLDL and its receptor VLDLR play critical roles in cardiovascular disease [13,17–19], and VLDLR's role in lipoprotein internalization and subsequent catabolism is well established [17,26]. Strikingly, the level of *Vldlr* mRNA, previously reported to be very lowly expressed in liver [26], was markedly higher in pericentral hepatocytes and in female mice (Fig. 2A). On the contrary, *Ldlr* expression was comparable in both sexes. At the protein level, immunostained sections of fresh frozen livers isolated every 4 h confirmed that VLDLR is pericentrally confined, with much stronger immunoreactivity in female tissue, and lowest signal in females at ZT22 (Fig. 2B; SFig. 10-11). Moreover, we observed a rhythm in the localization pattern of VLDLR, with cytoplasmic immunoreactivity at the fasting-feeding transition and predominantly membrane localization of the VLDLR signal at the feeding-fasting transition in both sexes (SFig. 2B), suggesting a temporal rhythm of VLDL capture and internalization.

Hepatic *Vldlr* upregulation by the commonly prescribed fenofibrate, a PPARα agonist, is indispensable for TAG lowering by fenofibrate [26]. Fenofibrate is associated with modest hepatic biochemical abnormalities in 5%-10% patients, and rare severe complications or development into DILI [27]. The pathologies could arise from impaired spatiotemporal compartmentalization of lipid metabolism [1]. After 5 days of fenofibrate treatment at therapeutic doses, we observed upregulated VLDLR pericentrally, with an increased spread further towards the periportal zone. The relative increase in VLDLR immunoreactivity was larger in males, however, it did not reach the native level in females at ZT10 (SFig. 10-11). Additionally, fenofibrate also increased female VLDLR abundance at ZT22, and male abundance at both ZT10 as well as ZT22. These effects may contribute towards sex-dependent outcomes of fenofibrate treatment [28,29].

Contrary to pericentral *Vldlr*, *Apoe* and *Tm6sf2*, involved in TAG secretion via lipidation of VLDL [30,31], as well as *Apoa4*, involved in TAG secretion and VLDL expansion [32], show higher periportal levels and higher expression in females in the scRNA-seq. *Apoc2*,

found on VLDL particles, was also higher periportally. Both APOA4 and APOC2 are physiologically important for recognition by the lipoprotein lipase (LPL) and its enzymatic activity, allowing LPL to hydrolyze TAGs carried by lipoproteins [33–35]. Thus, we identified a periportal bias of genes involved in VLDL generation, though *Apob*, lipidated to form VLDL, does not follow that pattern, but shows attenuated expression in the midlobular region (Fig. 2A). Of note, *Lpl* itself is pericentrally biased, and *Hsd17b13*, described as a protein associated with lipid droplets [36], shows robust periportal expression.

To assess the implications on the spatial properties of VLDL assembly, we employed transmission electron microscopy (TEM) on livers from 3 female and 3 male mice at ZT2. This time was antiphasic to cytoplasmic VLDLR immunoreactivity and coincided with the postprandial VLDL assembly [37,38]. Our optimized stainings allowed us to visualize VLDL-containing vesicles, localized at the Golgi, which were abundant periportally, but scarce pericentrally in both sexes (Fig. 3A, SFig. 12). The identification of these VLDL-containing vesicles was based on their electron density in TEM and well-established specific morphology [37,39], as well as on their known pathway of assembly and subcellular localization [40,41]. For accurate quantification of VLDL-containing vesicles in 3D cellular volumes, we employed scanning electron microscopy (SEM), showing a 2-fold periportal to pericentral VLDL ratio (Fig. 3B). These data indicate a periportal generation of carriers loaded with VLDL particles, consistent with spatial patterns of gene expression, and indicating spatial compartmentalization of VLDLR-mediated lipoprotein catabolism and VLDL generation. EM also revealed larger and differently shaped periportal mitochondria, which we reconstructed in 3D, fitting with a zonated mitochondrial transcript fraction observed previously [3] and found here (SFig. 13).

Intravenous injection of DiI-labeled VLDLs results in their accumulation in the liver (SFig. 14). Functionally, VLDLs are transporters of TAGs, delivering them to peripheral tissues for energy production. Mouse bulk lipidomics [42] revealed that over multiple conditions TAGs were higher in female liver while males showed higher circulating and spleen TAGs (SFig. 15). Higher male circulating TAG and APOB levels were also reported in humans [43,44]. These observations could be explained by a shift of TAGs to the liver in female mice, fitting with our model of higher hepatic VLDL uptake, possibly explaining why clearance of circulating VLDL-associated TAGs in humans is faster in women [16,45].

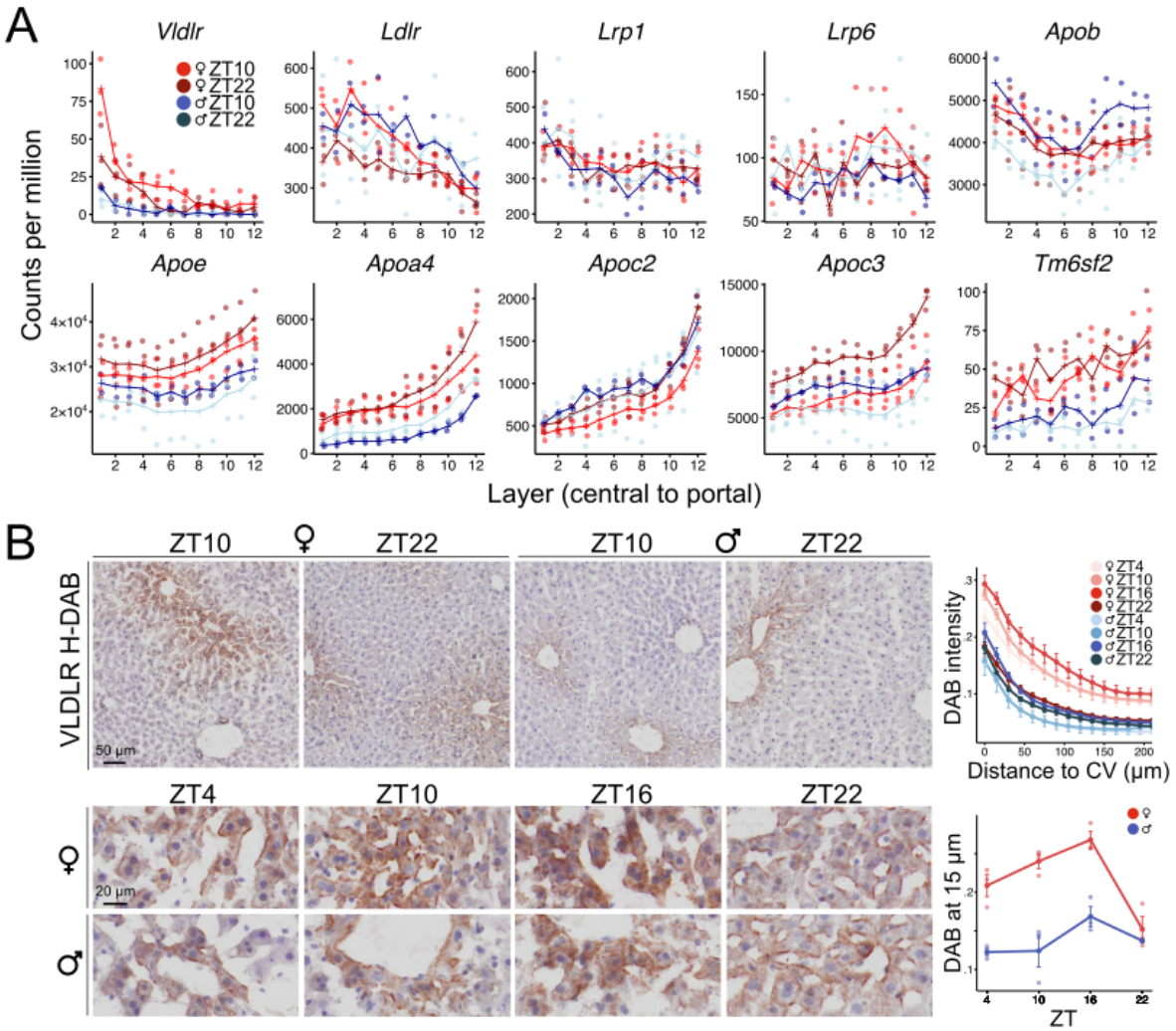

Figure 2: ***Pericentral and sex-dimorphic Vldlr expression.*** *(A) scRNA-seq revealed sexually dimorphic and pericentral expression of Vldlr. In females, the expression is lower at ZT22. Other lipoprotein receptors, Ldlr, Lrp1 and Lrp6, do not exhibit sexual dimorphism. Conversely, genes involved in VLDL generation, Apoe, Apoa4, Apoc2, Apoc3 and Tm6sf2, show periportal bias. Apob shows attenuated mRNA counts in the midlobular region (n = 11). (B) H-DAB staining shows pericentral confinement of VLDLR, with more intensive immunoreactivity in females. Male and female immunoreactivity is cytoplasmic at ZT10 and ZT16 while more membrane-localized at ZT22 and ZT4. Quantification of DAB staining shown as relative signal in concentric areas of 15 µm around the central vein (CV), or quantification of DAB signal at the distance of 15 µm from the central vein at different time points, errors represent SEM between biological replicates (n = 24).*

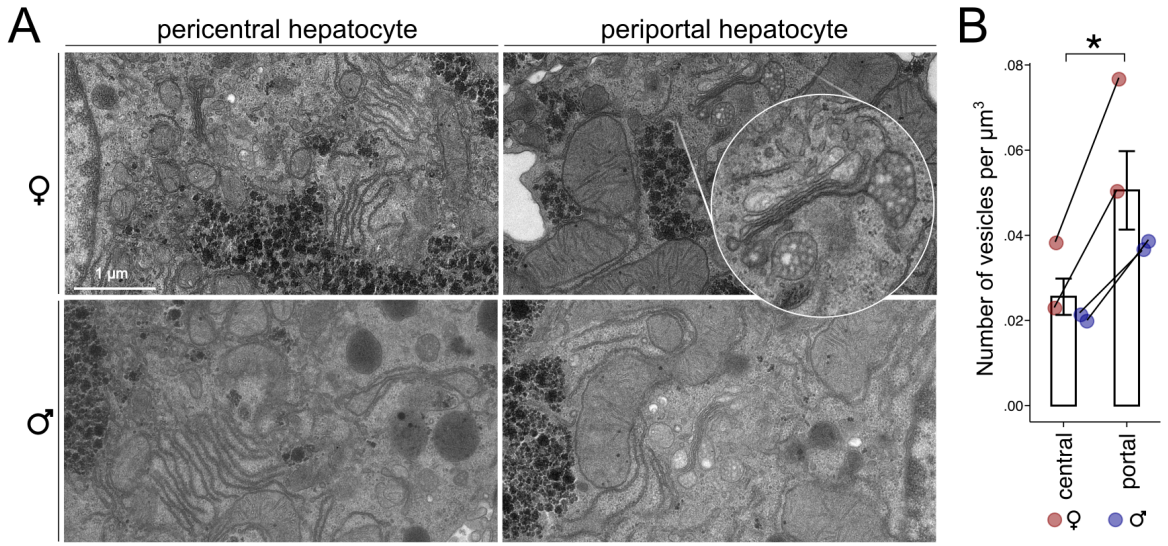

Figure 3: ***Periportal VLDL generation.*** *(A) Transmission EM images of periportal and pericentral hepatocytes. Periportal hepatocytes are rich in vesicles loaded with low density particles, whereas pericentrally these vesicles are scarce in both females and males. The scale bar represents 1 µm (n = 6 mice). (B) Scanning EM allowed quantification of vesicles loaded with VLDLs in > 40000 µm^3 of pericentral and periportal hepatic tissue, revealing an approximately 2-fold periportal to pericentral ratio of VLDL-loaded carriers (n = 4 mice, p = 0.017, paired t-test).*

2.3 VLDLR in humans recapitulates pericentral confinement and higher abundance in women

To investigate whether our findings are conserved in humans and to address the controversial low hepatic *VLDLR* [17,26], we compared *VLDLR* mRNA levels in 40 human tissues across hundreds of human donors from the Genotype-Tissue Expression (GTEx) program [25,46]. Additionally, we compared VLDLR protein abundance across 21 tissues [47]. While the liver showed approximately 4-fold lower mRNA compared to most assessed tissues, on the protein level, hepatic VLDLR levels were comparable to those in other organs, with the exception of the heart, where its abundance was approximately 5-fold higher (Fig. 4, SFig. 16). In comparison, hepatic *LDLR* mRNA is higher, but its protein abundance is similar. In the case of both receptors, the observed disconnection between mRNA expression and protein levels suggests abundant posttranscriptional regulation. The tissue-specific abundances of both receptors likely point to their distinct roles in either energy management or biosynthetic precursor shuttling (SFig. 16).

Next, we stratified the expression of *VLDLR* by sex, age and body mass index (BMI). Hepatic *VLDLR* mRNA was higher in premenopausal (40-49 years) female donors compared to males. The difference was lost in obese and in the postmenopausal (50-59 years) and

age-matched individuals. There were no differences between groups in *APOB* or *APOE*, but there was a trend of higher *LDLR* levels in young men (Fig. 3; SFig. 17).

Immunostaining of FFPE sections from 33 human donors (S. Table 4) confirmed a pericentral localization of VLDLR. Corresponding H&E stained slides were assessed by a pathologist to exclude the presence of significant macrovesicular and microvesicular steatosis. In a subset, a prominent pericentral deposition of lipofuscin was present. To exclude the possibility that a significant part of the signal in the VLDLR immunohistochemistry was due to lipofuscin, additional immunohistochemical stains using a purple chromogen were performed in a subset (Fig. 4C; SFig. 18-24).

We observed a generally higher premenopausal women VLDLR immunoreactivity compared to age matched men. Similarly to mRNA, the difference was lost between the postmenopausal and male age-matched donors, and intraindividual variability was more apparent in this age group. Contrary to mRNA, on the protein level, highest VLDLR levels were observed in premenopausal women, and these dropped after menopause, fitting with observed increases in circulating VLDL, LDL and triglycerides in postmenopausal women [48,49]. Taken together, the robust mouse data allowed us to identify a pericentral confinement of hepatic VLDLR in humans, with higher mRNA and protein levels in young women compared to men.

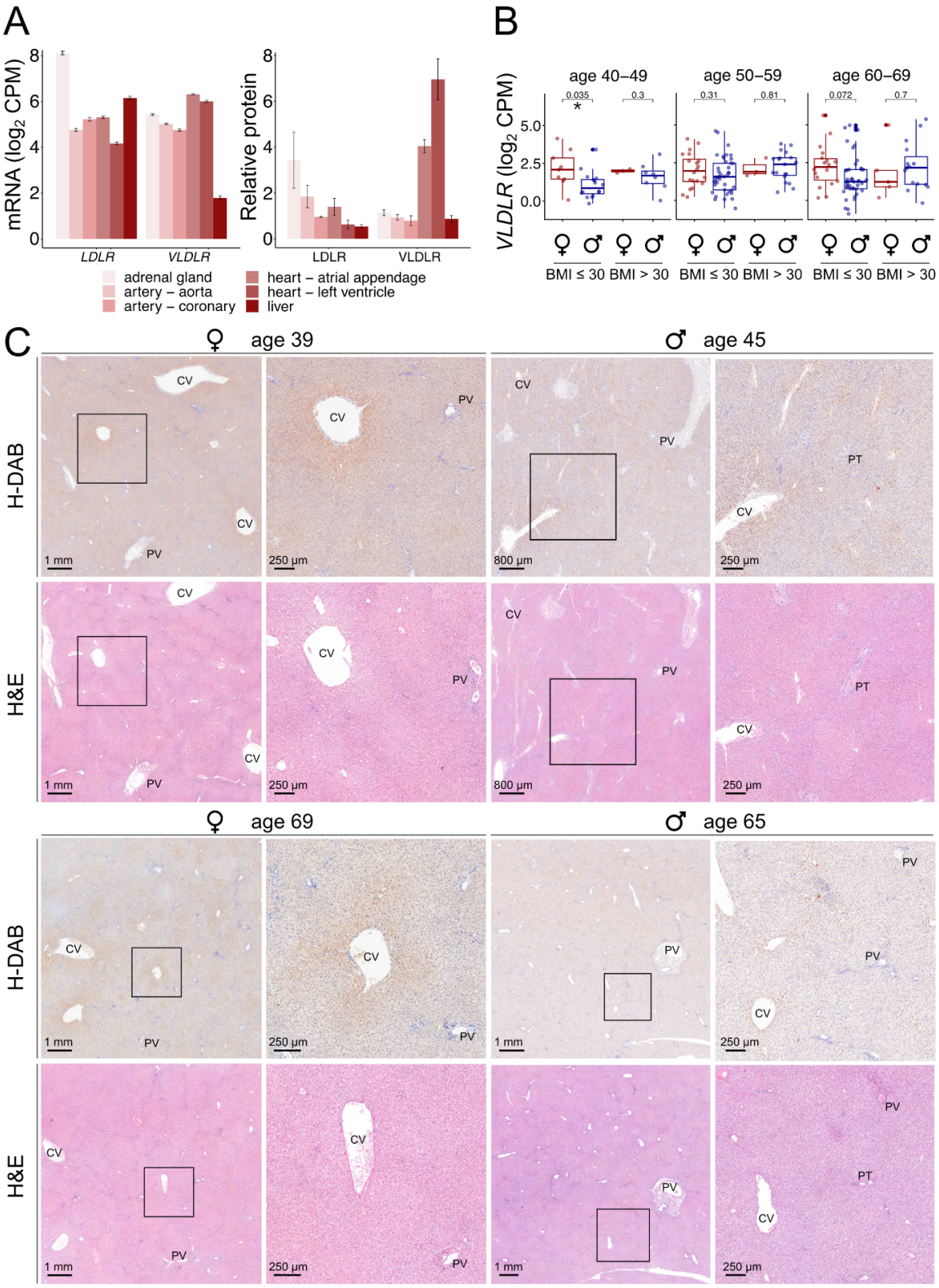

Figure 4: ***VLDLR expression and immunoreactivity in human liver tissue.*** *(A) Relative mean mRNA levels from bulk RNA-seq (left panel; error bars represent SEM) and relative mean protein levels from bulk proteomics (right panel; reanalysis of data from ref. 47; error bars represent SEM) in human tissue. While hepatic VLDLR mRNA levels are lower, the VLDLR protein abundance is comparable to that of LDLR in the liver. Hepatic VLDLR protein abundance is comparable to that in the aorta and coronary artery. (B) Stratification of bulk RNA-seq*

reveals 88% higher VLDLR mRNA levels in 40-49 year-old premenopausal women compared to age-matched males in the BMI < 30 group, or 122% higher after outlier removal (more than 3 standard deviations from the group mean). In obese individuals with a BMI > 30, this difference was lost. The center line represents the mean, error bars represent the interquartile range, p-values were calculated with a t-test, without outlier removal. (C) H-DAB VLDLR immunostaining and corresponding diagnostic H&E sections from the same FFPE block. Samples were grouped by sex and age, with the younger group consisting of premenopausal female donors and age matched males. Based on the quantified DAB signal, non-pathological samples with the median immunoreactivity were chosen for representative images. For each representative sample, a lower magnification overview and a higher magnification image are shown. Squares mark the magnified area. H-DAB staining shows VLDLR immunoreactivity around the central veins in all samples. Samples with median immunoreactivity in each group suggest highest DAB stain intensity in the premenopausal female donor (n = 33 donors). CV - central vein, PV - portal vein, PT - portal tract.

3. DISCUSSION

Our analysis revealed spatiotemporal and sex-dimorphic regulation of lipoprotein metabolism, with (patho-)physiological implications. Whereas atherosclerosis is marked by inflammatory processes, it is initiated with lipid accumulation within arteries [50]. VLDL particles are the main culprit [13,14,51], and they are precursors of other atherosclerotic lipoproteins, including VLDL remnants and LDL. Additionally, there is ample evidence that VLDLR plays a key role in trafficking of lipoproteins, including the atherogenic lipoprotein A and chylomicron remnants, such that gene therapy to increase hepatic *VLDLR* was proposed to mitigate atherosclerosis [17,18,26]. We uncovered higher *VLDLR* in female mice and young women compared to males, with explicit sublobular domains of VLDLR immunoreactivity, suggesting pericentral VLDL uptake. In parallel, we uncovered a periportal bias of VLDL generation, resulting in a spatial separation of VLDL assembly and VLDLR-mediated VLDL and remnant uptake. Moreover, our immunostainings demonstrate temporal patterns of cytoplasmic VLDLR immunoreactivity, antiphasic to proposed rhythms of VLDL generation from bulk lipidomics [38], suggesting spatiotemporal compartmentalization of VLDL assembly and catabolism.

This contrasts with the earlier view that VLDL generation occurs pericentrally [52] and suggests that healthy young women likely have a higher capacity of intrahepatic recycling of VLDL compared to similarly aged men. Our findings could contribute to explaining lower levels of circulating VLDL, remnants and LDL as well as APOB and TAG in women and the sexual dimorphism in coronary heart disease [44,53]. In fact, plasma clearance of VLDL-associated TAGs is much higher in women than men, and in men plasma TAG levels are related to VLDL TAG secretion, whereas in females they are related to VLDL TAG clearance [16,45]. For such a striking phenotype, a large organ has to be involved as a considerable metabolite turnover is needed. Importantly, the liver has discontinued

capillaries, which allow for large lipoproteins to come in contact with the hepatic parenchyma, supporting the role of hepatic VLDLR in systemic lipoprotein catabolism.

Hepatic *Vldlr* in mice can be upregulated with fenofibrate through PPARα [19,54–56] activation, suggesting a conserved mechanism within the fibrate class, which likely translates to humans. Fibrates have shown success in some, but fallen short of expectations in other clinical trials [57], with different outcomes between men and women [29]. This calls for a strategy to determine which patients would benefit from fibrate-mediated *VLDLR* upregulation and which from other strategies, including the attenuation of VLDLR degradation with the emerging class of PCSK9 inhibitors [58]. Speculatively, *VLDLR* expression could already be closer to the plateau in certain groups, resulting in limited success of fibrate administration. In certain individuals, *VLDLR* could be upregulated by higher circulating lipids that drive PPAR activation. Sex, age, BMI and type of dyslipidemia could be considered for stratification, as fibrates primarily reduce TAGs.

Together, our results suggest a mechanism underlying sex-dimorphic atherosclerotic cardiovascular disease, based on a hepatic cycle of periportal formation and pericentral uptake of VLDL.

Acknowledgements

We thank Stéphanie Clerc-Rosset for TEM imaging, Olivier Burri for producing a script for DAB immunostaining quantification, Gian-Filippo Mancini for histological processing of tissues, Roy Combe for whole organ fluorescence imaging, Irene Centeno-Ramos for coordinating experiments on human tissue, and Prof. Giovanni D'Angelo for advice. The work was supported by a Swiss National Science Foundation grant.

Author contributions

T. M. and F. N. conceived and designed the experiments. T. M. performed most of the experiments, analyzed the data and prepared the figures. C. G. and A. S. performed the computational analysis, A. M. assessed the human tissue. J. B. and G. K. planned and analyzed electron microscopy experiments. J. S. D. planned and oversaw the histology. T. M. and F. N. wrote the manuscript.

Disclosures

The authors declare no competing interests.

Code availability

The codes that support the findings of this paper are available from the corresponding author upon request.

4. MATERIALS AND METHODS

Animal experimentation

All animal experimentation was done according to local laws, and approved by the veterinary office of the Canton of Vaud, Switzerland. Mice were housed under a 12 h light-dark cycle and temperature of 21 ± 2 °C, with ad libitum access to food and water. The time of a perturbation is denoted with *zeitgeber time* (ZT), in accordance with the nomenclature in chronobiology, and ZT0 and ZT12 refers to the time of the switching on or off of lights, respectively. Experiments were performed with 129S6/SvEv (Taconic) mice, abbreviated as 129S in the manuscript. Additional and comparative data from C57BL/6 and CD-1 strains came from previous work, as described in corresponding method and result sections.

Handling of human tissue

All human tissue handling, storage and human experimentation was performed according to local laws, and the work was approved by the Cantonal commission of Vaud for ethics in human research. All participants signed a written consent form. The tissue (S. Table 2) was obtained from the Tissue Biobank Bern (TBB) of the University of Bern, with the criteria to exclude steatotic tissues. The TBB sectioned FFPE at 4 µm and flash frozen samples at 10 µm thickness. Further manipulation of the tissue was performed in house, except H&E staining and scanning, which was done at the University of Bern.

Analysis of mouse bulk sequencing data

C57BL/6 RNA-seq data was reanalysed from Weger et al. [7]. Differential expression analysis was previously performed using DESeq2 [59].

Analysis of human mRNA data(GTEx RNA-seq)

Raw gene read count data was obtained from GTEx V8 (2017-06-05_v8_RNASeQCv1.1.9, dbGaP Accession phs000424.v8.p2). For each tissue, genes with fewer than 10 counts across the samples were excluded. Counts were normalized based on library size and scaled using the edgeR TMM method [60], followed by conversion to counts per million (CPM).

After the addition of a pseudo-count of 0.25, CPM values were log-transformed (log_2). In each tissue, information on sex, age, and BMI was retrieved from the dbGap metadata (phs000424.GTEx.v8.p2.c1.GRU) for every individual. Differential expression was assessed between age, sex and BMI groups using a t-test.

scRNA-seq

Isolation and cryopreservation of cells

For perfusions, a peristaltic pump was used to withdraw buffered solutions from a water bath, kept at 42 °C, via a system of medical grade silicone tubing. The tubing led to a Graham condenser, which was heated with a circulating water flow from the water bath, utilizing a separate pump. The solutions exited the Graham condenser vial medical grade silicone tubing, which was connected via Luer adapters to a butterfly needle. The system ensured that all solutions had an approximate temperature of 37 °C at the tip of the butterfly needle. To perform the perfusion, mice were euthanized with 150 mg per kg pentobarbital. Upon absence of reflexes, the cadavers were opened and the butterfly needle, connected to the peristaltic pump system, was inserted into the inferior vena cava and clamped into place with a surgical hemostat. The perfusion pump was started and the portal vein was immediately cut to prevent an increase of pressure within the liver. First, to flush the blood, the perfusion was performed for 3 min using a buffer without collagenase. Subsequently, the mice were perfused for 3 min with a solution containing collagenase. Intact livers were isolated, placed into approx. 15-20 ml DMEM : F12, and cells released by breaking the Glisson's capsule. Next, straining through a 70 µm mesh and enrichment for hepatocytes based on centrifugation (50 G for 5 min, with a low breaking speed) was performed. For the centrifugation, each sample was split in two: one falcon was immediately stored as described below. The other falcon was used for resuspension of the pellet, and cell counting and viability assessment (trypan blue), followed by another round of centrifugation. After isolation, we implemented a isopentane cell freezing protocol to preserve cells isolated at the two precise time-points, allowing us to prepare sequencing libraries at a later point. Briefly, after centrifugation, the whole falcon tube containing the pellet enriched for hepatocytes was dipped into isopentane, precooled to -80 °C. The cell viability assessment upon thawing (see below) confirmed the feasibility of the freezing protocol.

Preparation of libraries for single-cell sequencing

The cryopreservation reduced hands-on time significantly. It also enabled us to thaw the cells immediately before loading onto the microfluidics chip of the scRNA-seq kit, reducing cell sticking and appearance of doublets in the dataset. Briefly, cells stored in 50 ml falcon

tubes were placed on ice, and DMEM : F12 (1 : 1) medium with 10% FBS, cooled at 4 °C, was immediately added to a final concentration of 2×10^6 cells per ml. Within 5 min, the cells were gently resuspended with a 50 ml serological pipette. The addition of 10% FBS to the medium reduced cell aggregation and the larger serological pipette reduced shear stress on the cells. The cell concentration and viability was assessed and the cells were immediately mixed with the 10x Genomics reagents and loaded on a pre-prepared (glycerol already in empty rows) 10x Genomics Chromium chip. Library preparation was performed using the 10x Genomics Chromium v3 kit according to manufacturer's instructions. The assessment of viability post freezing showed virtually no loss of cells.

Analysis of mouse scRNA-seq data

Filtering and clustering

Raw sequencing data were aligned to the mouse genome (mm10) using CellRanger (6.1.2). Intron and exon counts were computed using Velocyto [61]. From all sequenced GEMs, cells were selected on a per-sample basis by evaluation of the intronic fraction of individual GEMs (refer to [62]). GEMs with no or low introns were removed for each sample. A cutoff between a low and mid intron distribution was set on a per-sample basis, but at 8.5% for most samples. As hepatocytes are highly metabolically active with a high percent of mitochondrial genes in the transcriptome [63], and nonparenchymal cells have lower mitochondrial fractions, a filter of < 40% mitochondrial reads was set. Initial analysis was performed using the Seurat 4.3.0 package. Briefly, samples were normalized (sctransform) and integrated (features = 3000) and the cells clustered based on a t-distributed stochastic neighbor embedding (t-SNE) dimensionality reduction and Louvain algorithm (resolution = 0.5). This allowed us to identify individual cell types. For quantifications of gene expression in identified clusters of individual celly types, non-integrated transcripts (UMIs) were normalized to the total cytoplasmic gene count (excluding mitochondrial genes) since the mitochondrial fraction changes in function of cell type and lobular zone in hepatocytes. We identified a subcluster of hepatocytes that separated from others by low expression of secreted proteins and which exhibited a low mitochondrial fraction. To split the hepatocytes into those with low and high mitochondrial fractions, a cutoff of 3% mitochondrial genes was chosen. For the high mitochondrial gene subpopulation of hepatocytes (≥ 3%), a lobular position was calculated (spatial reconstruction), as described below. The pseudo-bulk calculations were done on all samples, with 3 biological replicates per condition. For spatial reconstruction and subsequent plotting of expression profiles, a male ZT22 sample was removed due to lower transcript levels.

Spatial reconstruction of hepatocyte zonation profiles from scRNA-seq

We developed a probabilistic model to assign a one-dimensional spatial position to every cell based on the expression patterns of established zonation marker genes in individual cells [3,23,24]. The initial set of markers, taken from ref. 22, included *Pck1*, *Aldh1b1*, *Ctsc*, *Sds*, *Hal*, *Hsd17b13*, *Cyp2f2* as portal and *Oat*, *Cyp2e1*, *Lect2*, *Cyp2c37*, *Gulo*, *Cyp2a5*, *Glul*, *Aldh1a1*, *Cyp1a2*, *Slc22a1*, *Slc1a2* as central markers. The spatial latent lobule coordinate *x* was determined by maximizing the likelihood of the observed raw counts, given *x* and other model parameters. We used a negative binomial noise model for the read counts to best capture the fluctuations of scRNA-seq data [59]. The expectation of the negative binomial distribution for a cell c and gene g in sample s was modeled by $\mu_{gcs} = N_{cs} exp(a_g x_{cs} + b_{gs})$, where a_g and b_{gs} are gene-specific slope and intercept coefficients. Note that the gene slopes a_g are the same across all samples, while intercepts $b_{g,s}$ can be sample dependent. Thus we assumed that there are landmark zonation genes with invariant slopes across all the samples, and these define the lobular coordinates. Finally, N_{cs} is the number of unique molecular identifiers (UMI) captured for cell c in sample s. The dispersion parameter α was also fitted and it is unique across all samples and cells. The fitted values of the dispersion parameter (0.076 for the initial gene set and 0.096 for the enriched one) are quite low indicating minimal overdispersion, closely approximating a Poisson model.

This model displays inherent symmetries without further constraints on the parameter, in fact the model has rank-deficiency $s + 1$. One symmetry is a scaling invariance as the expected values μ_{gcs} only depends on the product $a_g x_{cs}$. We broke this symmetry by setting the slope a_g of a selected gene (*Cyp2e1*) to 1 (which also sets the directionality of the central to portal axis, i.e. portal genes have a positive slope). The remaining s symmetries concern translational invariance: the shifting of all cells in a sample by the same quantity q_s redefines the intercept $b'_{gs} = b_{gs} + a_g q_s$. To set the reference, we fixed q_s such that cells expressing the highest central marker genes (e.g. *Glul*) were aligned across all the samples.

We initialized cell positions x_{cs} using principal component analysis (PCA). Specifically, the projection on the first principal component (PC) was used. This choice was justified since it was clear that the first principal component correctly separated central and portally expressed genes. The initial gene parameters, a_g and b_{gs} were fitted to the PCA positions through negative binomial regression. Once we obtained these complete sets of initial values, we used gradient descent to optimize positions and gene parameters together.

In a second step, once the cell coordinates were estimated as described above, we expanded our set of reference zonation markers to enhance the robustness of the spatial assignment. Initially, we chose a subset of 400 genes that showed the most significant deviations from a linear trend in the coefficient of variation (CV) versus mean plot, as the initial set of marker genes exhibited substantial divergence from this trend. Next, we fitted the model's slopes and intercepts for every gene, while keeping the cell positions *x* previously fitted with the smaller/initial set of genes fixed. Large positive or negative slopes, corresponding to central or portal genes, allowed us to identify potential zonation markers. Here to account for inter-mouse variability, we let the slope coefficient be sample dependent ($\mu_{gcs} = N_{cs} exp(a_{gs} x_{cs} + b_{gs})$) which was not the case in the first model. Finally, we chose genes that had the highest slope's mean to variance ratio (highest signal to noise) across the different mice. The final enriched set of genes included *Ctsc*, *Aldh1b1*, *Pigr*, *Serpina1d*, *Apoc2*, *Hal*, *Gc*, *Hsd17b13*, *Itih4*, *Apoc3*, *Hpx*, *Hsd17b6*, *Apoa4*, *Sds*, *Serpina1b*, *Serpinc1*, *Alb*, *Cyp2f2*, *Pck1* as portal and *Rnase4*, *Glul*, *Oat*, *Cyp2c37*, *Airn*, *Lect2*, *Slc22a1*, *Cyp2e1*, *Cyp7a1*, *Gm30117*, *Aldh1a1*, *Cyp2c50*, *Lhpp*, *Cyp1a2*, *Slc1a2*, *Cyp2a5*, *Pon1*, *Slco1b2*, *Cyp2c54*, *Mgst1*, *Gulo*, *Lgr5* as central markers.

The plotted expression profiles (Fig. 1-2) were generated by binning the 1D coordinates into 12 bins, representing layers of hepatocytes around the central vein. The expression is represented as counts per million (CPM), normalized by the total gene count excluding mitochondrial genes.

Model selection on mouse scRNA-seq data

After spatial inference of hepatocytes, the spatial expression profiles were further characterized by a model selection approach. Genes with > 300 total reads in at least one condition were retained. For these 6235 genes, we employed the 'glmmTMB' R package [64] to fit a generalized linear mixed-effects (GLMM) model (with a log link function), accounting for negative binomial noise and utilizing the Broyden–Fletcher–Goldfarb–Shanno optimization method. To address numeric instability for genes not expressed in at least one condition (less than 10 total counts), we performed an imputation using random draws from a negative binomial distribution with mean $\mu = e^{-4}$ and dispersion 0.1. Spatial coordinates across all samples were normalized to the range of 0 to 1 for consistent comparisons. Ten models, with incrementally increased complexity, were considered for each gene. These models included fixed effects, with intercepts and slopes being either sex, or time-specific, along with possible interaction terms, and random effects for the intercept and slope in each animal. The library size, computed by summing all gene counts except mitochondrial genes, served as an offset in the GLMM. A Bayesian Information Criterion (BIC) was employed, assigning genes to the model exhibiting the lowest BIC. To optimize computational efficiency,

we parallelized the analysis at the gene level using the 'mclapply' function from the parallel R package. We kept the estimated fixed effect coefficients from the best-fitting model for each gene. Note that the current simplest model with linear dependency in the positions was not designed to capture genes with peaks in the midlobular region, of which previous analysis identified only very few [24]. Moreover, the assignment to complex models with interacting effects of sex and time on the shape of zonation profiles did not yield many genes (15 genes in models 9 and 10, BIC, S. Table 3), and for those models the assignments seem sensitive to noise. Therefore we did not consider those genes further.

Fenofibrate injections

Fenofibrate was injected intraperitoneally at 80 mg per kg body mass for 5 straight days, at ZT0. Due to its low solubility and instability in water, fenofibrate was dissolved in DMSO in 10x working concentration and frozen at -20 °C. Upon thawing of the solution, medical grade 0.9% NaCl was added to the final volume, resulting in a suspension (rather than solution), which was shaken before loading into the syringe and injecting. Tissue was isolated at two time points that followed the 5th injection, ZT10 and ZT22.

Histology

Collection and freezing of mouse tissue

Tissue for histology and scanning lipidomics was isolated, placed into cryo molds, covered with 2% carboxymethylcellulose (CMC) in distilled water (prepared by sonication of CMC in water), and placed into a deep section of dry ice, allowing for even and quick freezing. The tissue from VLDL-DiI tracer studies was placed on a cryo mold and placed into a deep section of dry ice for flash freezing, without the addition of CMC. The tissue was subsequently cryosectioned at 10 µm, placed on glass slides and stored at -80 °C until processing.

Immunofluorescence of global zonation markers

Triple immunofluorescence was performed manually on mouse liver 10 µm fresh frozen sections. Tissues were fixed with 4% PFA for 15 min at RT before permeabilization with 0.1% Tween in 1x PBS for 10 min. After 30 min of blocking with 1% BSA in 1x PBS, primary antibodies were incubated simultaneously overnight at 4 °C: rabbit anti-CYP2E1 (Abcam ab28146, 1 : 300), mouse anti-GS/GLUL (Santa Cruz sc-74430, clone E-4, 1 : 100) and goat anti-E-CAD (R&D systems AF478, 1 : 200). After washes with 1x PBS, secondary antibodies were applied simultaneously for 40 min at RT: donkey anti-rabbit Alexa568

(Thermo Fisher A10042, 1 : 1000), donkey anti-mouse Alexa647 (Thermo Fisher A31571, 1 : 1000) and donkey anti-goat Alexa488 (Thermo Fisher A11055, 1 : 1000). Sections were counterstained with DAPI and mounted with FluoromountG (Bioconcept 0100-01).

Imaging

Imaging was done with the Olympus VS120 and Olympus VS200 slide scanners and Leica DM5500 widefield microscope. Images were subsequently analyzed using QuPath and FIJI software suites, with additional packages, as described in corresponding sections.

Electron microscopy (EM)

Two different preparation methods were used to image VLDL particles in hepatocytes with electron microscopy. A first, optimized for visualizing cell ultrastructure at high resolution with transmission electron microscopy, appears to leave the VLDL particles unstained, therefore light gray. While the second method, optimized for imaging cell ultrastructure in serial images with block face scanning electron microscopy, renders the particles heavily stained, therefore black (SFig. 13). This dark staining of these particles is similar to that seen in previous methods where the tissue is stained using osmium tetroxide as the primary fixative [37].

Mouse perfusion

After euthanasia, and immediately after the heart had stopped beating, adult mice were perfused with a buffered mix of 1.2% glutaraldehyde and 2.0% paraformaldehyde in 0.1 M phosphate buffer (pH 7.4). The livers were removed 2 hours after the perfusion had finished, and were then vibratome sectioned at 100 µm thickness.

Preparation of liver tissue for transmission electron microscopy

These sections were then washed with cacodylate buffer (0.1 M, pH 7.4), postfixed for 40 min in 1.0% osmium tetroxide with 1.5% potassium ferrocyanide, and then 40 min in 1.0% osmium tetroxide alone. They were then stained for 30 min in 1% uranyl acetate in distilled water before being dehydrated through increasing concentrations of ethanol and then embedded in Durcupan ACM (Fluka, Switzerland) resin. The slices were finally mounted between two glass slides and placed in an oven for 24 hours at 65 °C. Once the resin had hardened, a region of interest from a single slice was cut away from the rest and glued to a blank resin block, with cyanoacrylate glue, and thin (50 nm thick) serial sections were cut with a diamond knife (Diatome, Switzerland). These were collected onto pioloform support films on single slot copper grids and contrasted with lead citrate and uranyl acetate. Images were taken with a transmission electron microscope at 80 kV (Tecnai Spirit, FEI Company with Eagle CCD camera).

Preparation of liver tissue for serial block face scanning electron microscopy

The vibratome slices of fixed liver tissue were postfixed in potassium ferrocyanide (1.5%) and osmium (2%), then stained with thiocarbohydrazide (1%) followed by osmium tetroxide (2%) alone. They were finally stained overnight in uranyl acetate (1%), washed in distilled water at 50 °C before being stained with lead aspartate at pH 5.5 at the same temperature. The slices were then dehydrated in increasing concentrations of alcohol and embedded in Durcupan resin and hardened at 65 °C for 24 h. Once hardened, the region of interest was cut away from the rest of the slice with a scalpel blade. This piece was glued to an aluminum holder with conductive cement and then placed inside the scanning electron microscope (Merlin, Zeiss NTS) integrated with an in-chamber ultramicrotome device (3View, Gatan). The ultramicrotome was set to remove 50 nm thick slices from the surface of the block and images of the region were taken after each removal. An imaging voltage of 1.7 kV was used and a pixel size of 7 nm. Backscattered electrons were collected with a Gatan backscattered electron detector with a pixel dwell time of 1 µs.

Tracer studies

129S6/SvEv (Taconic) mice, aged 4-6 months, were placed under an IR lamp 5 min before tail vein injections to ensure vasodilation and visualization of the vein. The mice were then placed into a restrainer, and injected with 200 µl of the buffered solution of VLDL particles containing the DiI (1,1'-dioctadecyl-3,3,3'3'-tetramethylindocarbocyanine perchlorate) fluorophore (Kalen Biomedical). After 15 min, the mice were injected with 150 mg per kg body mass pentobarbital, and dissected 5 min later. At that time-point, all reflexes were absent in all of the mice, and death was confirmed with decapitation. Blood was removed from the liver by perfusion with PBS via the spleen, whereas other imaged organs were cut open and flushed of blood in PBS. Organs were collected, immediately imaged in the IVIS in vivo imaging system (PerkinElmer), in combination with the Living Image 4.5 software.

5. REFERENCES

1. Martini, T., Naef, F. & Tchorz, J. S. Spatiotemporal Metabolic Liver Zonation and Consequences on Pathophysiology. *Annu. Rev. Pathol.* **18**, 439–466 (2023).
2. Martini, T. *et al.* The Hepatic Monocarboxylate Transporter 1 (MCT1) Contributes to the Regulation of Food Anticipation in Mice. *Front. Physiol.* **12**, (2021).
3. Droin, C. *et al.* Space-time logic of liver gene expression at sub-lobular scale. *Nat. Metab.*

3, 43–58 (2021).

4. Kettner, N. M. *et al.* Circadian Homeostasis of Liver Metabolism Suppresses Hepatocarcinogenesis. *Cancer Cell* **30**, 909–924 (2016).
5. Gachon, F. Physiological function of PARbZip circadian clock‐controlled transcription factors. *Ann. Med.* **39**, 562–571 (2007).
6. Rinn, J. L. & Snyder, M. Sexual dimorphism in mammalian gene expression. *Trends Genet.* **21**, 298–305 (2005).
7. Weger, B. D. *et al.* The Mouse Microbiome Is Required for Sex-Specific Diurnal Rhythms of Gene Expression and Metabolism. *Cell Metab.* **29**, 362-382.e8 (2019).
8. Sugathan, A. & Waxman, D. J. Genome-Wide Analysis of Chromatin States Reveals Distinct Mechanisms of Sex-Dependent Gene Regulation in Male and Female Mouse Liver. *Mol. Cell. Biol.* **33**, 3594–3610 (2013).
9. Goldfarb, C. N., Karri, K., Pyatkov, M. & Waxman, D. J. Interplay Between GH-regulated, Sex-biased Liver Transcriptome and Hepatic Zonation Revealed by Single-Nucleus RNA Sequencing. *Endocrinology* **163**, bqac059 (2022).
10. Lawlor, D. A., Ebrahim, S. & Davey Smith, G. Sex matters: secular and geographical trends in sex differences in coronary heart disease mortality. *BMJ* **323**, 541–545 (2001).
11. Keng, V. W., Largaespada, D. A. & Villanueva, A. Why men are at higher risk for hepatocellular carcinoma? *J. Hepatol.* **57**, 453–454 (2012).
12. Andrade, R. J. *et al.* Drug-induced liver injury. *Nat. Rev. Dis. Primer* **5**, 58 (2019).
13. Balling, M. *et al.* VLDL Cholesterol Accounts for One-Half of the Risk of Myocardial Infarction Associated With apoB-Containing Lipoproteins. *J. Am. Coll. Cardiol.* **76**, 2725–2735 (2020).
14. Castañer, O. *et al.* Remnant Cholesterol, Not LDL Cholesterol, Is Associated With Incident Cardiovascular Disease. *J. Am. Coll. Cardiol.* **76**, 2712–2724 (2020).
15. Björnson, E. *et al.* Triglyceride-rich lipoprotein remnants, low-density lipoproteins, and risk of coronary heart disease: a UK Biobank study. *Eur. Heart J.* ehad337 (2023) doi:10.1093/eurheartj/ehad337.

16. Mittendorfer, B., Yoshino, M., Patterson, B. W. & Klein, S. VLDL Triglyceride Kinetics in Lean, Overweight, and Obese Men and Women. *J. Clin. Endocrinol. Metab.* **101**, 4151–4160 (2016).

17. Krauss, R. M., Lu, J. T., Higgins, J. J., Clary, C. M. & Tabibiazar, R. VLDL receptor gene therapy for reducing atherogenic lipoproteins. *Mol. Metab.* **69**, 101685 (2023).

18. Turunen, T. A. K. *et al.* Sleeping Beauty Transposon Vectors in Liver-directed Gene Delivery of LDLR and VLDLR for Gene Therapy of Familial Hypercholesterolemia. *Mol. Ther.* **24**, 620–635 (2016).

19. Perman, J. C. *et al.* The VLDL receptor promotes lipotoxicity and increases mortality in mice following an acute myocardial infarction. *J. Clin. Invest.* **121**, 2625–2640 (2011).

20. Adler, M., Korem Kohanim, Y., Tendler, A., Mayo, A. & Alon, U. Continuum of Gene-Expression Profiles Provides Spatial Division of Labor within a Differentiated Cell Type. *Cell Syst.* **8**, 43-52.e5 (2019).

21. Liang, Y. *et al.* Temporal analyses of postnatal liver development and maturation by single-cell transcriptomics. *Dev. Cell* **57**, 398-414.e5 (2022).

22. Fellous, T. G. *et al.* Locating the stem cell niche and tracing hepatocyte lineages in human liver. *Hepatology* **49**, 1655–1663 (2009).

23. Hildebrandt, F. *et al.* Spatial Transcriptomics to define transcriptional patterns of zonation and structural components in the mouse liver. *Nat. Commun.* **12**, 7046 (2021).

24. Halpern, K. B. *et al.* Single-cell spatial reconstruction reveals global division of labour in the mammalian liver. *Nature* **542**, 352–356 (2017).

25. Talamanca, L., Gobet, C. & Naef, F. Sex-dimorphic and age-dependent organization of 24-hour gene expression rhythms in humans. *Science* **379**, 478–483 (2023).

26. Gao, Y. *et al.* Upregulation of hepatic VLDLR via PPARα is required for the triglyceride-lowering effect of fenofibrate. *J. Lipid Res.* **55**, 1622–1633 (2014).

27. Ahmad, J. *et al.* Identification and Characterization of Fenofibrate-Induced Liver Injury. *Dig. Dis. Sci.* **62**, 3596–3604 (2017).

28. Yoon, M. *et al.* Fenofibrate regulates obesity and lipid metabolism with sexual

dimorphism. *Exp. Mol. Med.* **34**, 481–488 (2002).

29. d'Emden, M. C. *et al.* Favourable effects of fenofibrate on lipids and cardiovascular disease in women with type 2 diabetes: results from the Fenofibrate Intervention and Event Lowering in Diabetes (FIELD) study. *Diabetologia* **57**, 2296–2303 (2014).

30. Luo, F., Oldoni, F. & Das, A. TM6SF2: A Novel Genetic Player in Nonalcoholic Fatty Liver and Cardiovascular Disease. *Hepatol. Commun.* **6**, 448–460 (2022).

31. Mahdessian, H. *et al.* TM6SF2 is a regulator of liver fat metabolism influencing triglyceride secretion and hepatic lipid droplet content. *Proc. Natl. Acad. Sci.* **111**, 8913–8918 (2014).

32. VerHague, M. A., Cheng, D., Weinberg, R. B. & Shelness, G. S. Apolipoprotein A-IV Expression in Mouse Liver Enhances Triglyceride Secretion and Reduces Hepatic Lipid Content by Promoting Very Low Density Lipoprotein Particle Expansion. *Arterioscler. Thromb. Vasc. Biol.* **33**, 2501–2508 (2013).

33. Weinstock, P. H. *et al.* Severe hypertriglyceridemia, reduced high density lipoprotein, and neonatal death in lipoprotein lipase knockout mice. Mild hypertriglyceridemia with impaired very low density lipoprotein clearance in heterozygotes. *J. Clin. Invest.* **96**, 2555–2568 (1995).

34. Goldberg, I. J., Scheraldi, C. A., Yacoub, L. K., Saxena, U. & Bisgaier, C. L. Lipoprotein ApoC-II activation of lipoprotein lipase. Modulation by apolipoprotein A-IV. *J. Biol. Chem.* **265**, 4266–4272 (1990).

35. Surendran, R. P. *et al.* Mutations in LPL, APOC2, APOA5, GPIHBP1 and LMF1 in patients with severe hypertriglyceridaemia. *J. Intern. Med.* **272**, 185–196 (2012).

36. Su, W. *et al.* Phosphorylation of 17β-hydroxysteroid dehydrogenase 13 at serine 33 attenuates nonalcoholic fatty liver disease in mice. *Nat. Commun.* **13**, 6577 (2022).

37. Claude, Albert. Growth and differentiation of cytoplasmic membranes in the course of lipoprotein granule synthesis in the hepatic cell. *The Journal of Cell Biology* **47**, 745–766 (1970).

38. Sprenger, R. R. *et al.* Lipid molecular timeline profiling reveals diurnal crosstalk

between the liver and circulation. *Cell Rep.* **34**, 108710 (2021).

39. Lieu, H. D. *et al.* Eliminating Atherogenesis in Mice by Switching Off Hepatic Lipoprotein Secretion. *Circulation* **107**, 1315–1321 (2003).

40. Tiwari, S. & Siddiqi, S. A. Intracellular Trafficking and Secretion of VLDL. *Arterioscler. Thromb. Vasc. Biol.* **32**, 1079–1086 (2012).

41. Hossain, T., Riad, A., Siddiqi, S., Parthasarathy, S. & Siddiqi, S. A. Mature VLDL triggers the biogenesis of a distinct vesicle from the *trans* -Golgi network for its export to the plasma membrane. *Biochem. J.* **459**, 47–58 (2014).

42. Surma, M. A. *et al.* Mouse lipidomics reveals inherent flexibility of a mammalian lipidome. *Sci. Rep.* **11**, 19364 (2021).

43. Seidell, J. C. *et al.* Fat distribution and gender differences in serum lipids in men and women from four European communities. *Atherosclerosis* **87**, 203–210 (1991).

44. Tabassum, R. *et al.* Lipidome- and Genome-Wide Study to Understand Sex Differences in Circulatory Lipids. *J. Am. Heart Assoc.* **11**, e027103 (2022).

45. Mittendorfer, B., Patterson, B. W. & Klein, S. Effect of sex and obesity on basal VLDL-triacylglycerol kinetics. *Am. J. Clin. Nutr.* **77**, 573–579 (2003).

46. Oliva, M. *et al.* The impact of sex on gene expression across human tissues. *Science* **369**, (2020).

47. Jiang, L. *et al.* A Quantitative Proteome Map of the Human Body. *Cell* **183**, 269-283.e19 (2020).

48. Karppinen, J. E. *et al.* Menopause modulates the circulating metabolome: evidence from a prospective cohort study. *Eur. J. Prev. Cardiol.* **29**, 1448–1459 (2022).

49. Watanabe, K. *et al.* Metabolic profiling of charged metabolites in association with menopausal status in Japanese community-dwelling midlife women: Tsuruoka Metabolomic Cohort Study. *Maturitas* **155**, 54–62 (2022).

50. Björkegren, J. L. M. & Lusis, A. J. Atherosclerosis: Recent developments. *Cell* **185**, 1630–1645 (2022).

51. Alaupovic, P., Mack, W. J., Knight-Gibson, C. & Hodis, H. N. The Role of

Triglyceride-Rich Lipoprotein Families in the Progression of Atherosclerotic Lesions as Determined by Sequential Coronary Angiography From a Controlled Clinical Trial. *Arterioscler. Thromb. Vasc. Biol.* **17**, 715–722 (1997).

52. Guzmán, M. & Castro, J. Zonation of fatty acid metabolism in rat liver. *Biochem. J.* **264**, 107–113 (1989).

53. Wang, X., Magkos, F. & Mittendorfer, B. Sex Differences in Lipid and Lipoprotein Metabolism: It's Not Just about Sex Hormones. *J. Clin. Endocrinol. Metab.* **96**, 885–893 (2011).

54. Inoue, T. *et al.* Cross-enhancement of ANGPTL4 transcription by HIF1 alpha and PPAR beta/delta is the result of the conformational proximity of two response elements. *Genome Biol.* **15**, R63 (2014).

55. Terada, M., Araki, M., Ashibe, B. & Motojima, K. GW501516 acts as an efficient PPARα activator in the mouse liver. *Drug Discov. Ther.* **5**, 176–180 (2011).

56. Zarei, M. *et al.* Hepatic regulation of VLDL receptor by PPARβ/δ and FGF21 modulates non-alcoholic fatty liver disease. *Mol. Metab.* **8**, 117–131 (2018).

57. Shipman, K. E., Strange, R. C. & Ramachandran, S. Use of fibrates in the metabolic syndrome: A review. *World J. Diabetes* **7**, 74–88 (2016).

58. Poirier, S. *et al.* The proprotein convertase PCSK9 induces the degradation of low density lipoprotein receptor (LDLR) and its closest family members VLDLR and ApoER2. *J. Biol. Chem.* **283**, 2363–2372 (2008).

59. Love, M. I., Huber, W. & Anders, S. Moderated estimation of fold change and dispersion for RNA-seq data with DESeq2. *Genome Biol.* **15**, 550 (2014).

60. Robinson, M. D., McCarthy, D. J. & Smyth, G. K. edgeR: a Bioconductor package for differential expression analysis of digital gene expression data. *Bioinforma. Oxf. Engl.* **26**, 139–140 (2010).

61. La Manno, G. *et al.* RNA velocity of single cells. *Nature* **560**, 494–498 (2018).

62. Muskovic, W. & Powell, J. E. DropletQC: improved identification of empty droplets and damaged cells in single-cell RNA-seq data. *Genome Biol.* **22**, 329 (2021).

63. Osorio, D. & Cai, J. J. Systematic determination of the mitochondrial proportion in human and mice tissues for single-cell RNA-sequencing data quality control. *Bioinformatics* **37**, 963–967 (2021).

64. Brooks, M., E. *et al.* glmmTMB Balances Speed and Flexibility Among Packages for Zero-inflated Generalized Linear Mixed Modeling. *R J.* **9**, 378 (2017).